PHYSICAL REVIEW RESEARCH **4**, L012030 (2022)

Letter

Sub-laser-cycle control of relativistic plasma mirrors

L. Chopineau,[1,2,*] G. Blaclard,[1,*] A. Denoeud,[1,2] H. Vincenti,[1] F. Quéré,[1] and S. Haessler[3,†]
[1]*LIDYL, CEA, CNRS, Université Paris-Saclay, CEA Saclay, 91191 Gif-sur-Yvette, France*
[2]*CEA, DAM, DIF, F-91297 Arpajon, France*
[3]*Laboratoire d'Optique Appliquée, Institut Polytechnique de Paris, ENSTA-Paris, Ecole Polytechnique, CNRS, 91120 Palaiseau, France*

(Received 29 July 2021; accepted 6 January 2022; published 11 March 2022)

We present measurements of high-order harmonics and relativistic electrons emitted into the vacuum from a plasma mirror driven by temporally shaped ultraintense laser wave forms, produced by collinearly combining the main laser field with its second harmonic. We experimentally show how these observables are influenced by the phase delay between these two frequencies at the attosecond timescale, and relate these observations to the underlying physics through an advanced analysis of 1D/2D particle-in-cell simulations. These results demonstrate that subcycle shaping of the driving laser field provides fine control on the properties of the relativistic electron bunches responsible for harmonic and particle emission from plasma mirrors.

DOI: 10.1103/PhysRevResearch.4.L012030

I. INTRODUCTION

Plasma mirrors are overdense plasmas created at the surface of laser-ionized optically flat solid targets. They are versatile optical devices for the manipulation of ultraintense femtosecond (fs) laser beams ($I_L \gtrsim 10^{16}\,\mathrm{W/cm^2}$). They are also considered as a promising path for the generation of intense attosecond light pulses through high-order harmonic generation (HHG) [1–5] as well as for laser-driven particle acceleration [6–9]. From a fundamental standpoint, plasma mirrors represent ideally simple testbeds for ultrahigh-intensity laser–plasma interaction physics because the dynamics is confined to a thin layer at the target surface where the plasma particles are directly exposed to the ultraintense laser field, without any prior alteration of this field [10,11].

Collective electronic motion at this plasma–vacuum interface on a sub-fs timescale plays a key role in this physics. When a p-polarized laser is focused on a solid target at intensities $I_L \gtrsim 10^{18}\,\mathrm{W/cm^2}$, the laser-driven electron motion becomes relativistic and can be described by a push–pull process [12–14], repeating once per driving laser period. The incident laser field first pushes electrons into the plasma, piling up a dense electron bunch and creating a restoring internal plasma field. As the laser field changes sign, the combined plasma and laser fields accelerate the electron bunch to a relativistic velocity toward the vacuum. This can induce drastic temporal modulations to the reflected laser wave, which sensitively depend on the electron bunch properties and dynamics [15–20]; key physical parameters are the bunch charge, velocity, and spatial extent. In the spectral domain, these periodic temporal modulations result in HHG. We will refer to this process as *Relativistic Oscillating Mirror* (ROM) in the following.

While most of the electrons then get pushed back into the plasma, a fraction of them are expelled into the vacuum at relativistic velocities. Their tight temporal locking with the laser field then lets them get further accelerated in the reflected laser field through *Vacuum Laser Acceleration* (VLA) [7]. This suggests a tight correlation of HHG and fast-electron emissions in the relativistic regime, which has indeed been observed experimentally [21,22].

While the understanding of this relativistic laser–plasma interaction physics has greatly advanced over the past two decades, the means of its experimental control have remained rather limited. To date, the main control knob is the scale length L_g of the plasma density gradient at the plasma–vacuum interface, $n(x) \propto \exp[-x/L_g(\tau)]$, which can be varied by adjusting the delay τ between a weaker ionizing prepulse and the main ultraintense driving pulse [10,11]. On the relevant sub-fs timescale, this is of course a static parameter. An adequately fast dynamic control could be achieved with a temporally tailored driving wave form. This concept has already had great success with strong-field dynamics driven on the single-atom level at much lower intensities $\sim 10^{14}\,\mathrm{W/cm^2}$ [23–27]. Its potential for relativistic plasma mirrors has recently been shown in numerical studies [28,29] that predicted significant enhancements of the HHG efficiency, which was shortly after confirmed in a first experiment [30]. However, no other observable than the angle-integrated HHG spectrum has been studied, leaving mostly unexplored the detailed attosecond control afforded by the additional degree of freedom of the driving optical cycle shape.

In this Letter, we present experiments where high-order harmonics as well as relativistic electrons are generated through the interaction of a plasma mirror with ultraintense

---

[*] These authors contributed equally to this work.

[†] stefan.haessler@ensta-paris.fr.

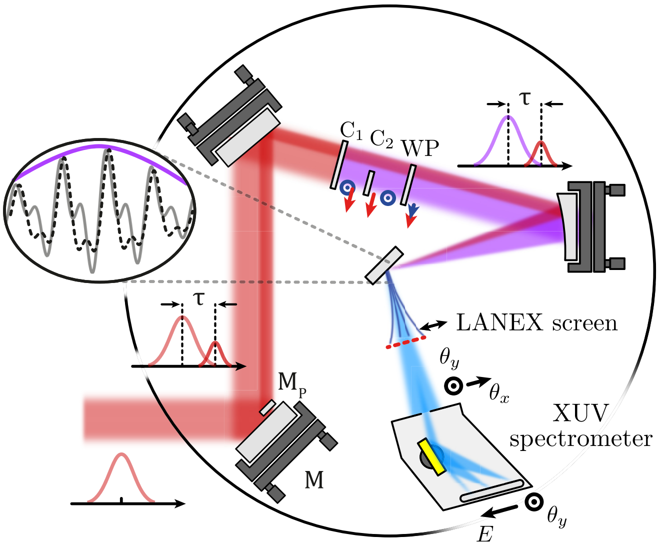

FIG. 1. (**a**) Experimental setup with the prepulse (red) and main pulse (purple) with adjustable relative delay τ as set by the two-part mirror M / M_P and the three crystals C_1, C_2, WP for two-color wave form generation (see text). The inset shows wave forms obtained for $\tau_{\phi,h} = 0$ (solid gray line) and $\tau_{\phi,e} = -T'/4$ (dashed black line).

temporally shaped optical cycles, generated by combining the fundamental laser field (ω_L) with its second harmonic ($2\omega_L$). By adjusting their relative phase, we can dynamically control the collective plasma electron motion on the sub-fs timescale. We simultaneously measure the angularly and spectrally resolved high-order harmonics generated around the specular direction, as well as the high-energy electron beam emitted into the vacuum. Finally, we relate these observations to the underlying physics through an advanced analysis of 1D/2D particle-in-cell (PIC) simulations.

II. EXPERIMENTAL SETUP

The experiments are carried out on the 100 TW-class Ti:sapphire laser UHI100 (LIDYL, CEA Saclay), delivering 25-fs pulses at central wavelength $\lambda_L = 800$ nm with an excellent temporal contrast $\gtrsim 10^{13}$ on a $\gtrsim 100$ ps timescale reached thanks to a double plasma mirror system [31]. Under these conditions, the maximum energy on target is ~ 0.5 J, distributed in a 65-mm-diameter near-top-hat beam. A deformable mirror coupled to a wave-front sensor (Imagine Optic) corrects aberrations thus optimizing the focal spot on target.

The optical setup preparing the pulse sequence sent on target is shown on Fig. 1. The scale length L_g of the plasma density gradient on the target surface, $n(x) \propto \exp[-x/L_g(\tau)]$, is controlled by a weak prepulse ($F \simeq 10^3$ J/cm^2 on target) at an adjustable delay τ before the main pulse [10]. The value of L_g was measured using spatial domain interferometry [11]. An aperture mask transmits the prepulse as well as a 33-mm-diameter top-hat main beam (limited by the available size of the calcite crystal mentioned below).

The two-color wave forms are generated by a combination of three transmissive optics [24,30] (see Fig. 1); part of the fundamental light with frequency ω_L is frequency-doubled to $2\omega_L$ in an 800-μm-thick KDP crystal (C_1; Gooch & Housego), which can be rotated away from the optimum phase-matching angle to reduce the conversion efficiency from its maximum of $\approx$25% down to zero. Due to the top-hat beam profile we suppose a spatially uniform SHG efficiency. The temporal walkoff due to dispersion is partly compensated by shortening due to the nonlinearity of SHG [30] so that we suppose a 35-fs pulse duration for the 2ω component.

The timing of the two color components is controlled by a 1.5-mm-thick calcite crystal (C_2; 35 mm × 35 mm; Berhard Halle Nachfl.) with its optic axis oriented at 45° to the crystal front surface and perpendicular to the fundamental's polarization axis. As shown in Appendix A, small rotations of the crystal about this axis lead to quasilinear shifts of the relative group delay τ_g and phase delay τ_ϕ of the two color components. Their temporal pulse envelopes are well overlapped for a 4.3° incidence angle on the calcite crystal. Scanning the calcite angle in small steps ($\sim 0.01^\circ$) over a 0.13°-wide range around this position shifts the group delay in total by $\approx$1.7 fs and the phase delay by $\tau_\phi = 1.34$ fs, the latter corresponding to $T' = 2\pi/2\omega_L$, i.e., one period of the second harmonic. Such a rotation therefore scans the full range of two-color optical-cycle shapes with excellent temporal stability and reproducibility while keeping the pulse envelopes well overlapped.

Finally, a 273-μm-thick quartz wave plate (WP; 6.5λ at 400 nm, 3λ at 800 nm; Eksma Optics) rotates the polarization direction of the second harmonic so as to be parallel to that of the fundamental. The total energy of the one- or two-color pulses on target is $\approx$125 mJ.

Both the prepulse and the two-color main pulse are p-polarized and focused by a $f = 200$-mm off-axis parabola onto a fused-silica target at 58° angle of incidence. The measured diameter (FWHM in intensity) of the optimized focal spot of the fundamental color component is 5.6 μm, whereas it is estimated to 3.3 μm for the second harmonic beam, leading to on-target peak intensities of 5×10^{18} and 3.5×10^{18} W/cm^2, respectively.

Two diagnostics for the plasma mirror emission have been implemented as displayed in Fig. 1. First, the spatial profile of the electron beam, $S_e(\theta_x, \theta_y)$, was measured using an insertable LANEX screen placed at 150 mm from the target and imaged by a CCD camera. This scintillating screen is protected with a 13-μm-thick aluminium foil and thus detects only electrons with energies $\gtrsim$0.15 MeV. The high-harmonic emission, $S_h(\omega, \theta_y)$, was characterized using an angularly resolved XUV spectrometer with an angular acceptance of 200 mrad.

III. Experimental Results

A. Single-color (ω_L) driver

As a first step, we used a driving field of frequency ω_L only, obtained by rotating the KDP (C_1) crystal by 7° away from the optimum phase-matching angle, thus completely suppressing SHG while retaining the same $\approx$125 mJ pulse energy on target. We measured the evolution of the experimental observables with the gradient scale length L_g under otherwise equal interaction conditions to the subsequent

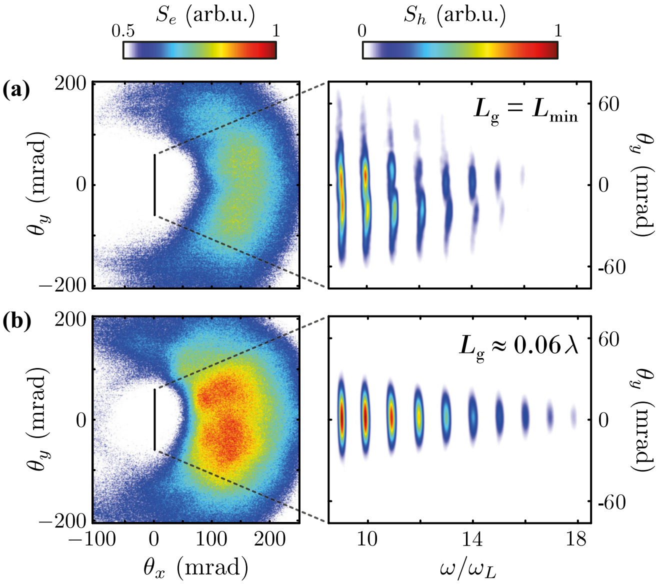

FIG. 2. Angular emission pattern of accelerated electrons (left) and angularly resolved harmonic spectrum (right) obtained with the minimal gradient scale length $L_g \lesssim \lambda_L/50$ (**a**) and with a gradient scale length optimizing both ROM HHG and vacuum-laser-accelerated electron emission (**b**). The vertical black lines in the electron beam profiles mark the XUV spectrometer angular acceptance.

two-color experiments. Letting the prepulse arrive after the main pulse minimizes L_g to $\lesssim \lambda_L/50$, limited by the main pulse temporal contrast. As demonstrated earlier [10,32], such a steep gradient strongly favors harmonic generation by the *Coherent Wake Emission* (CWE) process [33]. This mechanism leads to a sharp spectral cutoff at the maximum plasma frequency given by the target material density ($\sim 20\omega_L$ for silica) as well as rather high divergence [34] and marked spatial modulations of the emitted beam. A smoother density gradient ($L_g \approx \lambda/16$) provides optimal conditions for the ROM process [10,21,32], which at moderately relativistic driving intensities lead to lower divergence, spatially smooth beams [10,35,36]. Figure 2 shows this striking spatial difference in the measured HHG spectra. This evidences a transition from CWE to ROM harmonics with increasing L_g, although the spectra do not extend beyond the CWE spectral cutoff in our weakly relativistic regime ($a_0 \approx 1.5$). For the high-energy electron emission, also shown in Fig. 2, we find a correlation of the ejected charge with the ROM efficiency, i.e., both are maximized for $L_g \sim \lambda_L/16$. The electron beam in the ROM conditions was very similar to that measured in previous experiments [7], with a distinctive hole in the spatial beam profile centered on the specular direction, resulting from the interaction between the ejected electrons and the reflected laser light during VLA. Both the ROM mechanism and the electron acceleration benefit from the charge separation field produced at longer gradients. Their correlation for sinusoidal, i.e. single-color, driving wave forms has been reported before [21,22] and interpreted in the framework of the push–pull model [13].

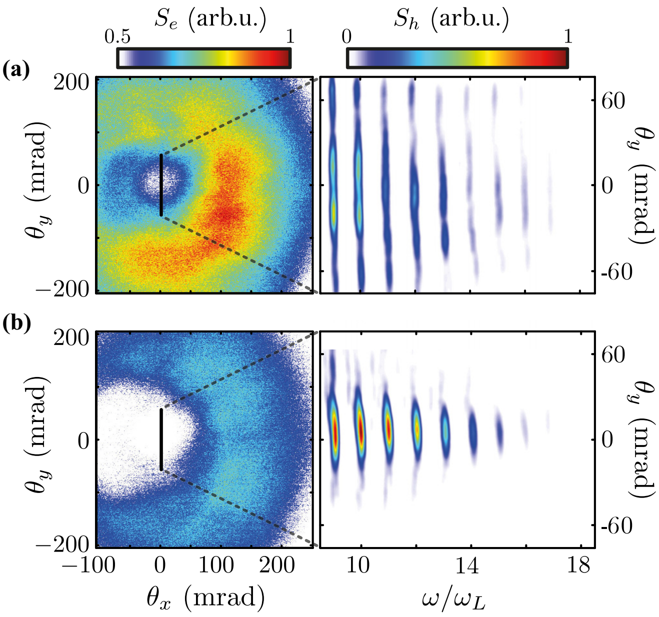

FIG. 3. Angular emission pattern of accelerated electrons (left) and angularly resolved harmonic spectrum (right) obtained with a gradient scale length $L_g \lesssim \lambda_L/50$ and for phase delays maximizing either the electron emission $\tau_{\phi,e}$ (**a**) or the high-order harmonic emission $\tau_{\phi,h}$ (**b**). The vertical black lines in the electron beam profiles mark the XUV spectrometer angular acceptance.

B. Two-color ($\omega_L + 2\omega_L$) driver

Using the temporally shaped two-color main beam, this clear correlation disappear; while the ejected electron charge varies very similarly with L_g as with the ω_L-only driver, the harmonic signal drops with increasing L_g to be finally absent around $L_g \sim \lambda_L/16$ (see Appendix B). This is the case for all two-color phase delays τ_ϕ. The parameters optimizing the HHG are thus no longer the same as those for relativistic electron emission, which is a first indication that the two-color driver modifies the plasma mirror dynamics.

This is further corroborated by the measurement of the electron and harmonic signals for the shortest gradient ($L_g \lesssim \lambda_L/50$) as a function of the ω_L–$2\omega_L$ phase delay τ_ϕ, i.e., of the optical cycle shape. The main experimental findings are shown in Fig. 3 by presenting the angular emission pattern of relativistic electrons $S_e(\theta_x, \theta_y)$ and the angularly resolved harmonic spectrum $S_h(\omega, \theta_y)$ in the cases where τ_ϕ is optimized for either the high-energy electrons or the high-order harmonics. Under our interaction conditions, we find clearly distinct optima for both observables. In particular, when the optical-cycle shape maximizes the electron charge [Fig. 3(a)], a highly divergent harmonic beam is reminiscent of that obtained in the CWE regime, whereas this beam becomes much less divergent and brighter in the other case [Fig. 3(b)]. This suggests that these harmonics are now generated via the ROM process, which had not been observed with the ω_L-single-color driver for such a short gradient (see Fig. 2). We conclude that on top of a less-bright CWE background, the ROM harmonic generation shows an on–off oscillation as a function of the driving optical cycle shape. No significant change in

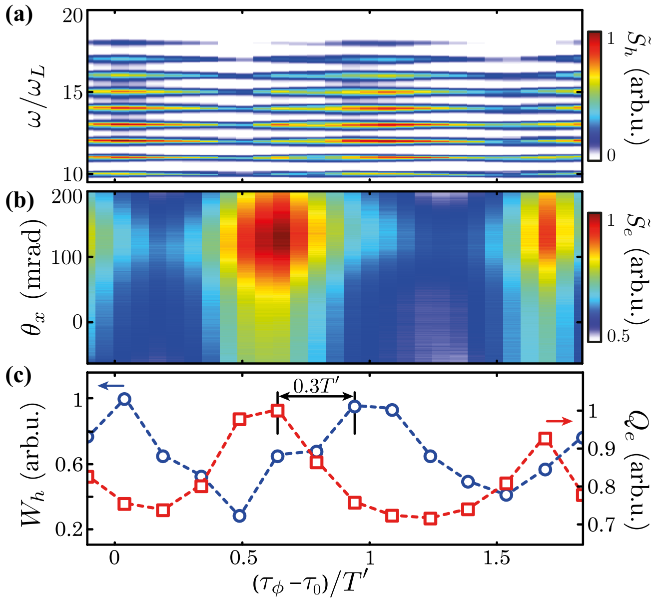

FIG. 4. Experimental harmonic spectrum $\tilde{S}_h$ (**a**) and accelerated electron beam profile $\tilde{S}_e$ (**b**) in the incidence plane as a function of the phase delay τ_ϕ (with an unknown experimental offset τ_0). The total high-harmonic energy W_h (blue circles) and electron charge Q_e (red squares) obtained by integration over the vertical dimensions in the panels above are plotted in panel (**c**). The ejected electron charge and the harmonic energy similarly oscillate but with optima shifted by $\simeq 0.3T'$. The experimental parameters are the same as in Fig. 3.

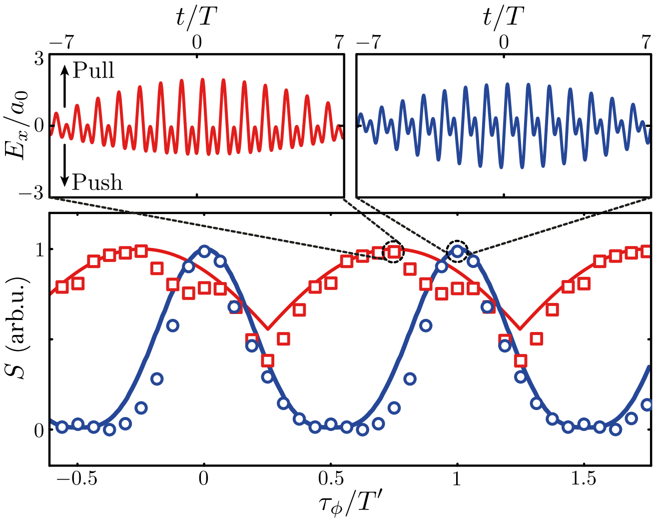

FIG. 5. Ejected electron charge (red squares) and high-order harmonic energy (blue circles) as a function of the phase delay τ_ϕ obtained from 2D PIC simulations. Full blue and red lines show the normalized heuristic model predictions $S(\tau_\phi)$ and $P(\tau_\phi)$ for E-field steepness ($n = 9$ here) and maximum pulling E field, respectively. The periodic modulations of these electronic and harmonic signals are shifted by $\simeq T'/4$. The insets above show the driving fields for maximum electron (left) and high-harmonic (right) emission. A positive-valued electric field pulls electrons out of the plasma into vacuum.

the electron spatial distribution other than the total charge is noticed.

The details of the experimental phase-delay dependence of the ejected electron charge and the harmonic emission are presented in Fig. 4. First, the emitted harmonic spectrum $\tilde{S}_h(\tau_\phi, \omega)$, shown in Fig. 4(a), represents the spectral intensity within the central 33-mrad-wide divergence cone, i.e., preferentially the ROM signal. The total high-harmonic energy $W_h(\tau_\phi)$ is obtained by integration over the presented spectral range ($\omega/\omega_L \in [10, 20]$). A clear modulation with a period $T' \approx 1.35$ fs is observed [Fig. 4(c)]. The electron beam angular profile $\tilde{S}_\mathrm{e}(\tau_\phi, \theta_\mathrm{x})$, obtained by integrating $S_e(\theta_x, \theta_y)$ over θ_y, is shown in Fig. 4(b). Further integration over θ_x yieds the emitted electron charge $Q_e(\tau_\phi)$ shown in Fig. 4(c). It oscillates with the same period as the harmonic signal, with lower contrast but nonetheless presenting clear extrema, which had never been observed before.

A striking finding is the dephasing of these periodic modulations: The optimum phase delays maximizing the ejected electron charge or ROM harmonic emission are shifted by $\approx 0.3T' = 0.4$ fs. Therefore, intense attosecond light pulses are not necessarily generated in correlation with high-charge electron beams, in contrast to experiments where control is solely achieved through the plasma density gradient scale length L_g. Temporally shaping the driving optical cycles thus adds a new dimension to the control parameter space, which allows optimizing properties of the ejected electron bunches whose effect on HHG outweighs that of their total charge.

As detailed in Appendix C, a ROM-HHG efficiency enhancement by a factor of ≈ 1.8 is also measured. Compared with earlier simulations [28,29] and experiments [30], this is much more modest here certainly due to our weakly relativistic intensity.

IV. NUMERICAL SIMULATIONS

A. 2D PIC

In order to gain insight into the dynamically controlled subcycle plasma dynamics, we turn to PIC simulations using the WARP+PXR code [37–43]. We consider a p-polarized incident laser pulse with electric field $E(t, \tau_\phi) = E_1(t)\sin(\omega_\mathrm{L} t) + E_2(t + \tau_\phi)\sin[2\omega_\mathrm{L}(t + \tau_\phi)]$, where $E_1(t)$ and $E_2(t)$ are 18 cycles long cosine-half-cycle envelopes (≈ 30 fs FWHM) with equal peak field strengths corresponding to a normalized vector potential of $a_0 = 1$ for an 800-nm wave. It impinges a solid target with gradient scale length $L_g = \lambda_L/50$ at 55° angle of incidence. The main results of 2D PIC simulations are summarized in Fig. 5, which show the ejected electron charge (only electrons with energies $\gtrsim 0.1$ MeV) as well as the high-order harmonic energy (harmonics 7 to 13; a region just before the CWE spectral cutoff for the simulated plasma density, cf. Appendix D) as a function of the phase delay τ_ϕ. Similarly to the experiments (although with higher contrast), we retrieve clear oscillations of the harmonic and electron signals with period T' and a relative shift by $\approx T'/4 = 0.35$ fs, in good agreement with the experimental results. Also shown in Fig. 5 are the incident driving wave forms that maximize the harmonic and electron emissions. In agreement with previous simulations done for similar as well as much higher laser intensities

[28–30], we find that the harmonic emission is optimized for a maximized wave form steepness in the change from the push to the pull phase (from negative to positive E- field). The emitted electron charge is found to be maximized, under our weakly relativistic conditions, rather for a wave form with the strongest possible field in the pull phase. This suggests a simple heuristic model: (i) A power-law dependence on the E-field steepness, $S(\tau_\phi) = (\max_t[\partial E(t,\tau_\phi)/\partial t|_{E(t)=0}])^n$, describes the harmonic signal modulation, and (ii) the maximum pulling field $P(\tau_\phi) = \max_t[E(t,\tau_\phi)]$ describes the electron charge modulation. Despite the extreme simplicity, these predictions are found to fit the signal modulations remarkably well, as shown in Fig. 5.

B. 1D PIC

To gain a deeper physical insight, we have performed 1D PIC simulations that allow performing larger ensemble runs with better statistics. The simulated conditions are kept the same as in the 2D case discussed above. For each driving wave form characterized by τ_ϕ, we analyze the electron bunch properties during the central optical cycle. At every instant, only those electrons with velocity $>0.1c$ toward the vacuum are selected to calculate their total charge, the bunch position as their spatial center of mass, and the bunch width as their spatial root-mean-square width. The time derivative of the bunch position gives the bunch velocity. We then select a time interval Δt_p for the pull phase, starting at the instant of maximum bunch charge and ending at the instant when either the bunch velocity vanishes or the bunch position has reached $z = 0.25\lambda_L$. The bunch properties plotted in Fig. 6 as a function of τ_ϕ are the bunch charge and velocity, both averaged over Δt_b, and the bunch width at the beginning of Δt_b. Note that this bunch charge is not directly that of the emitted VLA electron beam; the bunch analyzed here has not yet left the plasma and, as clearly visible in the insets in Fig. 6, part of it will turn back into the plasma during the subsequent pushing phase, in particular under our weakly relativistic conditions.

As in the 2D-simulations, the harmonic emission is maximized around $\tau_\phi = 0$ and thus for the fastest switch from pushing to pulling field. While this does not maximize the electron bunch charge, it creates both a well-compressed and a fast outgoing electron bunch, which are the key parameters for efficient ROM HHG [28,29]. The electron velocity alone, as considered in Ref. [30], is not a sufficient criterion; while it is also boosted by the wave forms with enhanced pulling field, around $\tau_\phi = -T'/4$ this comes at the expense of a weakened push phase and thus a less compressed electron bunch. This is the situation we find to be optimal for electron emission under our conditions. As apparent in the left inset in Fig. 6, the weaker field in the subsequent pushing phase lets a greater proportion of the bunch electrons fully escape the plasma with high velocity to be injected into the reflected laser field for VLA. Putting all emphasis on the pushing field strength ($\tau_\phi = +T'/4$) leads to the narrowest bunch, but at the expense of a smaller velocity. Finally, around $\tau_\phi = +T'/2$, where the harmonic emission is minimized, pushing and pulling peak fields are approximately balanced but the switch between the two is so slow that the compressed electron bunch breaks apart and is not effectively accelerated outward.

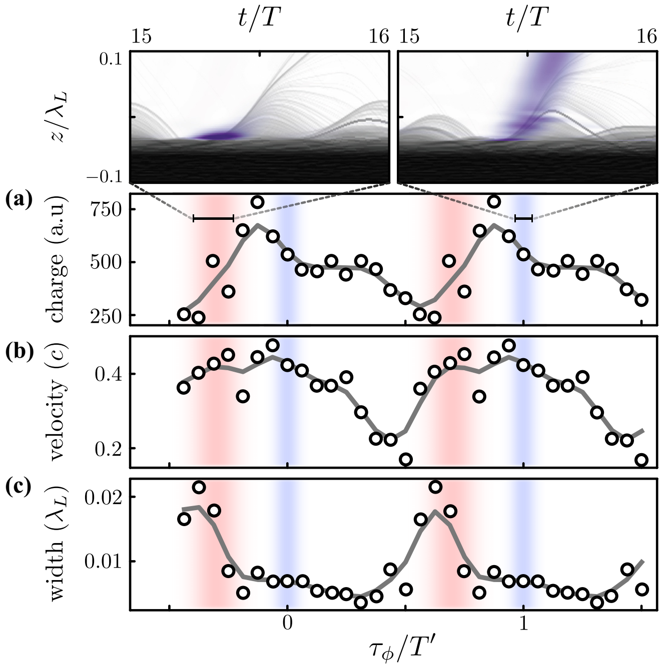

FIG. 6. Electron bunch properties during the pull phase as a function of the phase delay τ_ϕ extracted from 1D PIC simulations: Mean charge (**a**), mean velocity (**b**), and initial spatial width (**c**). Blue and red shadings mark the phase delay ranges maximizing harmonic and electron emissions, respectively, in the 2D simulations as shown in Fig. 5. The insets show the temporal evolution of the plasma electron density (grayscale color map in log scale) in each phase delay range, spatially resolved along the normal to the target surface. The emitted attosecond pulses are overlaid to this density map in purple. Note that the bunch charge (**a**) is not as that of the emitted VLA electron beam as displayed in Fig. 5.

V. CONCLUSIONS

In conclusion, we used ultraintense temporally shaped optical cycles to experimentally realize the dynamic control on the sub-fs timescale of collective plasma electron motion on plasma mirrors emitting high-order harmonics and relativistic electrons. The experimentally observed difference of the optimal two-color phase delays for harmonics and electrons under our conditions provides a strict gage for the comparison with PIC simulations. The fact that our simulations reproduce this difference thus significantly underpins the interpretations we draw from them, elucidating how the relative strength of pushing and pulling field half cycles and the rapidity of the switch between them controls the formation and outward acceleration of the dense electron bunches that lead to HHG and seed VLA.

These results illustrate the new possibilities opened by the attosecond steering of collective plasma electron motion driven by ultraintense multicolor wave forms. Our enhanced experimental characterization and fine control over extreme light-matter interactions together with their accurate modeling represent fundamental progress in high-field physics, of

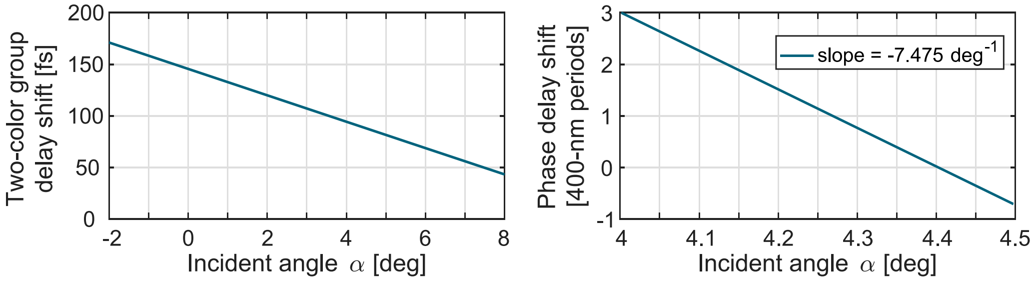

FIG. 7. Calculated relative group (left) and phase delays (right) between the 800-nm fundamental and the 400-nm second harmonic as a function of the incidence angle on the birefringent calcite crystal (C_2).

particular relevance, e.g., to the future quest of the Schwinger limit using PW-class lasers [44]. We expect that expanding this approach to other frequency combinations and polarization shaping will have a strong impact on the development of powerful plasma-based radiation and particle sources.

ACKNOWLEDGMENTS

We thank Aurélien Houard of LOA for lending the KDP crystal, Olivier Gobert of LIDYL for valueable discussions, and Fabrice Réau, Christophe Pothier and David Garzella for operating the UHI100 laser. This work was funded by the European Research Council under Contract No. 694596 of the European Union Horizon 2020 Research and Innovation Programme, the EquipEx Attolab (ANR-11-EQPX-005-ATTOLAB), the LabEx PALM (ANR-10-LABX-0039-PALM), and the Région Île-de-France (SESAME-2012-ATTOLITE). An award of computer time was provided by the INCITE programme (project PlasmInSilico). This research used resources of the Argonne Leadership Computing Facility, which is a DOE Office of Science User Facility supported under contract DE-AC02-06CH11357.

APPENDIX A: TWO-COLOR TIMING CONTROL

Figure 7 shows the calculated relative group and phase delays between the 800-nm fundamental and the 400-nm second harmonic as a function of the incidence angle on the birefringent calcite crystal (C_2). At 4.3° incidence angle, the $\approx$90 fs group delay induced by the propagation through the KDP (C_1) and subsequent WP is compensated. Scanning the calcite angle over a 0.13°-wide range around this position shifts the group delay in total by $\approx$1.7 fs and the phase delay by $\tau_\phi = 1.34$ fs, the latter corresponding to one period of the second harmonic. In other words, the pulse envelopes' relative timing shifts together with a simultaneous drift of the pulses' CEPs. Since the rotations remain very small, the resulting change of the pulse-envelope overlap remains negligible ($\approx$3.4 fs in the experimental scan over two modulation periods vs the pulse durations of $\approx$30 fs). We can therefore focus only on the scanned relative phase delay τ_ϕ of the two carrier waves (ω and 2ω), which is the quantity that governs the shape of optical cycle under the combined pulse envelope.

APPENDIX B: GRADIENT DEPENDENCE WITH THE TWO-COLOR DRIVER

Figure 8 shows HHG spectra and electron beam profiles measured with $\omega_L + 2\omega_L$ two-color driving wave forms with the phase delays τ_ϕ set so as to either optimize low-divergence ROM HHG or electron emission. For each driving wave form, the plasma gradient scale length L_g was scanned. Figure 8 shows the data for the same two scale lengths as in Fig. 2, i.e., the shortest accessible value $L_g \leqslant \lambda/50$ as well as $L_g \approx \lambda/16$ found optimal for *both* ROM HHG and electron emission with the ω_L-single-color driver. Here with both two-color driving wave forms, we find that while the ejected electron charge barely changes when increasing L_g up to $\approx \lambda/16$, the HHG signal rapidly drops and has almost completely vanished for the scale length $L_g \approx \lambda/16$. Thus the effect of the plasma density gradient scale length is different for single-color and two-color driving wave forms, and there is thus no longer a common set of optimal conditions for HHG and electron emissions in the two-color case.

APPENDIX C: EFFICIENCY COMPARISON

Figure 9 summarizes a comparison of the HHG efficiency obtained with a ω_L-single-color driver and $\omega_L + 2\omega_L$ two-color drivers. Clearly the HHG radiant intensities obtained with the single- and two-color beams are rather similar and we do not observe an order-of-magnitude efficiency boost as predicted in earlier simulations [28,29] and reported for the single previous experiment [30]. The reason may be the lower driving intensity in our case as evident from the fact that the HHG spectra in Ref. [30] extend beyond the CWE spectral cutoff at 30 eV (for SiO_2 targets) while ours do not.

Integrating the generated HHG emission spatiospectrally (from 15.2 to 28.5 eV and over a 33-mrad-wide cone around the spatial beam center, see the red boxes in Fig. 9), we find an HHG energy enhancement by a factor 1.8 for the "2-color best" case, i.e., the two-color driver with optimal phase delay τ_ϕ with the steepest initial plasma gradient [Fig. 9(b)] as compared with the "1-color ROM" reference case, i.e., the one-color driver (same on-target pulse energy of $\approx$125 mJ) with the optimized plasma gradient scale length $L_g \approx 0.06\lambda$ [Fig. 9(d)]. Relative to the same reference and in the same integration limits, the "1-color CWE" case yields a 1.3 times higher HHG energy (typical for the mildly relativistic regime near $a_0 = 1$, and the factor would increase further if a larger divergence cone were considered), while the "2-color worst"

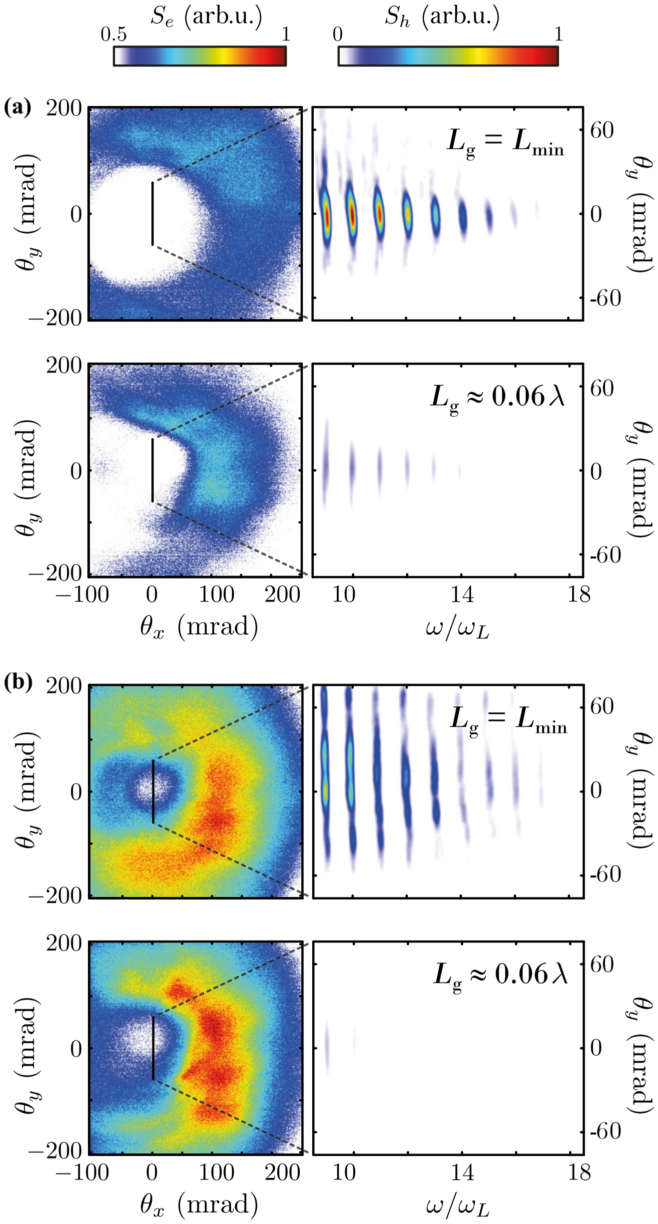

FIG. 8. Angular emission pattern of accelerated electrons (left) and angularly resolved harmonic spectrum (right) obtained with the same two gradient scale lengths as in Fig. 2 ($L_g \approx \lambda/50$ above and $L_g \approx \lambda/16$ below). The phase delay of the two-color driving wave forms is set such that it optimizes low-divergence ROM HHG emission (**a**) or fast electron emission (**b**). The vertical black lines in the electron beam profiles mark the XUV spectrometer angular acceptance.

case reduces the HHG energy by a factor of 0.6. We must, however, note that concluding from these observations on a useful ROM-HHG efficiency enhancement is made difficult by the presence of the high-divergence CWE background that remains present in the two-color case.

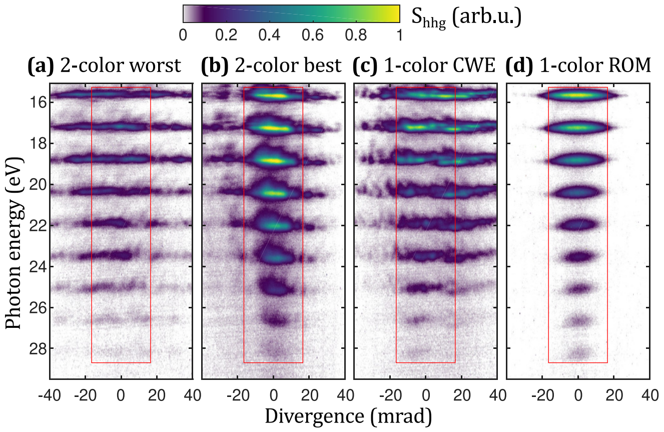

FIG. 9. Angularly resolved harmonic spectra obtained with minimal plasma gradient scale length $L_g \approx 0$ (**a**)-(**c**) and with $L_g \approx 0.06\lambda$ (**d**). Two-color ($\omega_L + 2\omega_L$) driver with a phase delay τ_ϕ minimizing [(**a**) "2-color worst"] or maximizing [(**b**) "2-color best"] the low-divergence ROM HHG emission. Single-color (ω_L) driver [(**c**) "1-color CWE;" (**d**) "1-color ROM"]. The linear color scale is the same in all panels such that the signals are quantitatively comparable. The red boxes in (**a**)–(**d**) mark the angular-spectral integration range for the efficiency comparison in the text.

Figure 10 summarizes a comparison of the detected electron beam profiles obtained with a ω_L-single-color driver and $\omega_L + 2\omega_L$ two-color drivers. Both for the steepest plasma gradient and for the scale length $L_g \approx 0.06\lambda$, optimal for ROM HHG emission as well as vacuum laser electron acceleration, we find very similar accelerated electron charges for a single-color driver and for two-color drivers with phase delay $\tau_{\phi,e}$ maximizing the electron charge. For the phase delay $\tau_{\phi,e} + T'/2$, minimizing the electron charge, the charge drops to about 65% of the charge obtained with $\tau_{\phi,e}$.

APPENDIX D: DETAILS ON PIC SIMULATIONS

The simulations presented in the paper were performed with the PIC code WARP+PXR that relies on a very accurate

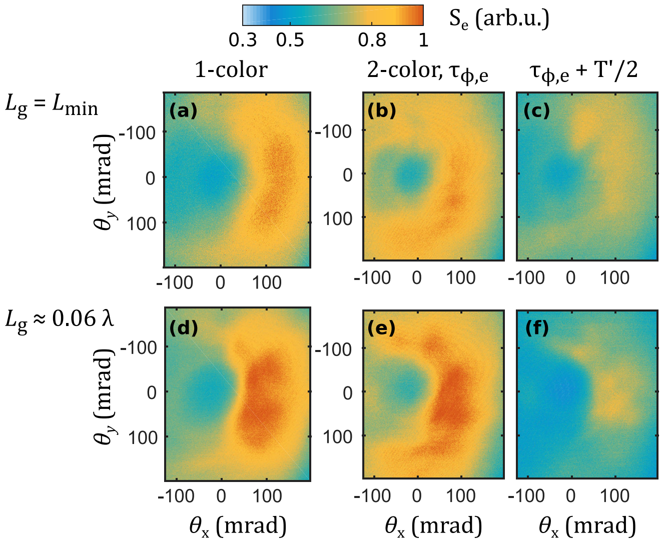

FIG. 10. Electron beam spatial profiles $S_(e)$ measured with minimal plasma gradient scale length $L_g \approx 0$ (**a**)–(**c**), with $L_g \approx 0.06\lambda$ (**d**)–(**f**), and with a single-color (ω_L) laser driver (**a**),(**d**); a two-color ($\omega_L + 2\omega_L$) driver with a phase delay τ_ϕ maximizing (**b**),(**e**) or minimizing (**c**),(**f**) the electron signal.

TABLE I. Numerical and physical parameters for simulations presented in the paper. Here θ is the angle of incidence, Δx and Δy are the spatial steps, Δt is the temporal step, c is the celerity of light, and n is an index to tune to modify the delay between the two-color components.

	1D	2D
Maxwell solver	PSATD	PSATD
Δx (Δy)	$\lambda/350$	$\lambda/160$
$c\Delta t$	Δx	Δx
Particles/Cell	500	5×5
a_0 (ω_L)	1	1
a_0 ($2\omega_L$)	0.5	0.5
Laser duration	≈30 fs	≈30 fs
Target density	220 n_c	220 n_c
L	$\lambda/50$	$\lambda/50$
θ	55°	55°
τ_ϕ	$nT_L/16$	$nT_L/16$

pseudospectral solver—PSATD (Pseudo-Spectral Analytic Time Domain)—where the fields are analytically integrated in Fourier space over a finite time step. The advantage of such a solver is that it largely mitigates most numerical effects; in particular, it suppresses all effects related to numerical dispersion, present in all finite-difference-based solvers. It then allows for a better convergence to the solution in term of computational resources [41]. Note that the two-color driving field $E(t,\tau_\phi) = E_1(t)\sin(\omega_L t) + E_2(t+\tau_\phi)\sin[2\omega_L(t+\tau_\phi)]$ used in the simulations is a simplified expression that neglects dispersion by assuming equal group and phase delay shifts: Both the envelope E_2 and the 2ω-carrier wave are shifted by τ_ϕ. Since the effect of the small relative group delay shift should be negligible (cf. the discussion in Appendix A), the difference of 0.36 fs per τ_ϕ period between experiment and simulations should also be negligible. Note also that in the simulations we only scanned over one 1.34-fs period of τ_ϕ and then duplicated the results to show two periods in Figs. 5 and 6 for better comparability with the experimental scan in Fig. 4 that was performed over two τ_ϕ periods. In Table I, we summarize the numerical and physical parameters used for our 1D and 2D simulations. Note that the CWE spectral cutoff in the experiments is at harmonic 20 while it is at harmonic 14 in the simulations due to the lower assumed bulk plasma density. The harmonic spectral range in Fig. 5 is chosen to be comparable to the experiment such that the CWE and ROM mechanisms contribute significantly. Note further that the 1D simulations were performed in a Lorentz boosted frame to emulate an angle of incidence θ of the laser on target.

[1] G. D. Tsakiris, K. Eidmann, J. Meyer-ter Vehn, and F. Krausz, Route to intense single attosecond pulses, New J. Phys. **8**, 19 (2006).

[2] B. Dromey, M. Zepf, A. Gopal, K. Lancaster, M. Wei, K. Krushelnick, M. Tatarakis, N. Vakakis, S. Moustaizis, R. Kodama *et al.*, High harmonic generation in the relativistic limit, Nat. Phys. **2**, 456 (2006).

[3] C. Thaury, F. Quéré, J.-P. Geindre, A. Levy, T. Ceccotti, P. Monot, M. Bougeard, F. Réau, P. d'Oliveira, P. Audebert *et al.*, Plasma mirrors for ultrahigh-intensity optics, Nat. Phys. **3**, 424 (2007).

[4] U. Teubner and P. Gibbon, High-order harmonics from laser-irradiated plasma surfaces, Rev. Mod. Phys. **81**, 445 (2009).

[5] L. Chopineau, A. Denoeud, A. Leblanc, E. Porat, P. Martin, H. Vincenti, and F. Quéré, Spatio-temporal characterization of attosecond pulses from plasma mirrors, Nat. Phys. **17**, 968 (2021).

[6] A. Macchi, M. Borghesi, and M. Passoni, Ion acceleration by superintense laser-plasma interaction, Rev. Mod. Phys. **85**, 751 (2013).

[7] M. Thévenet, A. Leblanc, S. Kahaly, H. Vincenti, A. Vernier, F. Quéré, and J. Faure, Vacuum laser acceleration of relativistic electrons using plasma mirror injectors, Nat. Phys. **12**, 355 (2016).

[8] Y. Tian, J. Liu, W. Wang, C. Wang, A. Deng, C. Xia, W. Li, L. Cao, H. Lu, H. Zhang, Y. Xu, Y. Leng, R. Li, and Z. Xu, Electron Emission at Locked Phases from the Laser-Driven Surface Plasma Wave, Phys. Rev. Lett. **109**, 115002 (2012).

[9] N. Zaïm, F. Böhle, M. Bocoum, A. Vernier, S. Haessler, X. Davoine, L. Videau, J. Faure, and R. Lopez-Martens, Few-cycle laser wakefield acceleration on solid targets with controlled plasma scale length, Phys. Plasmas **26**, 033112 (2019).

[10] S. Kahaly, S. Monchocé, H. Vincenti, T. Dzelzainis, B. Dromey, M. Zepf, P. Martin, and F. Quéré, Direct Observation of Density-Gradient Effects in Harmonic Generation from Plasma Mirrors, Phys. Rev. Lett. **110**, 175001 (2013).

[11] M. Bocoum, F. Böhle, A. Vernier, A. Jullien, J. Faure, and R. Lopez-Martens, Spatial-domain interferometer for measuring plasma mirror expansion, Opt. Lett. **40**, 3009 (2015).

[12] A. A. Gonoskov, A. V. Korzhimanov, A. V. Kim, M. Marklund, and A. M. Sergeev, Ultrarelativistic nanoplasmonics as a route towards extreme-intensity attosecond pulses, Phys. Rev. E **84**, 046403 (2011).

[13] M. Thévenet, H. Vincenti, and J. Faure, On the physics of electron ejection from laser-irradiated overdense plasmas, Phys. Plasmas **23**, 063119 (2016).

[14] A. Gonoskov, Theory of relativistic radiation reflection from plasmas, Phys. Plasmas **25**, 013108 (2018).

[15] R. Lichters, M. t. Vehn, and A. Pukhov, Short-pulse laser harmonics from oscillating plasma surfaces driven at relativistic intensity, Phys. Plasmas **3**, 3425 (1996).

[16] S. Gordienko, A. Pukhov, O. Shorokhov, and T. Baeva, Relativistic Doppler Effect: Universal Spectra and Zeptosecond Pulses, Phys. Rev. Lett. **93**, 115002 (2004).

[17] C. Thaury and F. Quéré, High-order harmonic and attosecond pulse generation on plasma mirrors: Basic mechanisms, J. Phys. B: At., Mol. Opt. Phys. **43**, 213001 (2010).

[18] an der Brügge and A. Pukhov, Enhanced relativistic harmonics by electron nanobunching, Phys. Plasmas **17**, 033110 (2010).

[19] J. M. Mikhailova, M. V. Fedorov, N. Karpowicz, P. Gibbon, V. T. Platonenko, A. M. Zheltikov, and F. Krausz, Isolated

Attosecond Pulses from Laser-Driven Synchrotron Radiation, Phys. Rev. Lett. **109**, 245005 (2012).

[20] M. R. Edwards and J. M. Mikhailova, The X-Ray emission effectiveness of plasma mirrors: Reexamining power-law scaling for relativistic high-order harmonic generation, Sci. Rep. **10**, 1 (2020).

[21] L. Chopineau, A. Leblanc, G. Blaclard, A. Denoeud, M. Thévenet, J.-L. Vay, G. Bonnaud, P. Martin, H. Vincenti, and F. Quéré, Identification of Coupling Mechanisms between Ultraintense Laser Light and Dense Plasmas, Phys. Rev. X **9**, 011050 (2019).

[22] S. Haessler, F. Böhle, M. Bocoum, M. Ouillé, J. Kaur, D. Levy, L. Daniault, A. Vernier, J. Faure, and R. Lopez-Martens, Relativistic high-harmonic generation and correlated electron acceleration from plasma mirrors at 1 kHz repetition rate, arXiv:2005.01343.

[23] R. Bartels, S. Backus, E. Zeek, L. Misoguti, G. Vdovin, I. Christov, M. Murnane, and H. Kapteyn, Shaped-pulse optimization of coherent emission of high-harmonic soft x-rays, Nature (London) **406**, 164 (2000).

[24] N. Dudovich, O. Smirnova, J. Levesque, Y. Mairesse, M. Y. Ivanov, D. Villeneuve, and P. B. Corkum, Measuring and controlling the birth of attosecond xuv pulses, Nat. Phys. **2**, 781 (2006).

[25] S. Haessler, T. Balčiunas, G. Fan, G. Andriukaitis, A. Pugžlys, A. Baltuška, T. Witting, R. Squibb, A. Zaïr, J.W.G. Tisch, J.P. Marangos, and L.E. Chipperfield, Optimization of Quantum Trajectories Driven by Strong-Field Waveforms, Phys. Rev. X **4**, 021028 (2014).

[26] C. Jin, G. Wang, H. Wei, A.-T. Le, and C. Lin, Waveforms for optimal sub-kev high-order harmonics with synthesized two-or three-colour laser fields, Nat. Commun. **5**, 4003 (2014).

[27] P. Wei, J. Miao, Z. Zeng, C. Li, X. Ge, R. Li, and Z. Xu, Selective Enhancement of a Single Harmonic Emission in a Driving Laser Field with Subcycle Waveform Control, Phys. Rev. Lett. **110**, 233903 (2013).

[28] M. R. Edwards, V. T. Platonenko, and J. M. Mikhailova, Enhanced attosecond bursts of relativistic high-order harmonics driven by two-color fields, Opt. Lett. **39**, 6823 (2014).

[29] M. R. Edwards and J. M. Mikhailova, Waveform-Controlled Relativistic High-Order-Harmonic Generation, Phys. Rev. Lett. **117**, 125001 (2016).

[30] M. Yeung, S. Rykovanov, J. Bierbach, L. Li, E. Eckner, S. Kuschel, A. Woldegeorgis, C. Rödel, A. Sävert, G. Paulus *et al.*, Experimental observation of attosecond control over relativistic electron bunches with two-colour fields, Nat. Photonics **11**, 32 (2017).

[31] A. Lévy, T. Ceccotti, P. D'Oliveira, F. Réau, M. Perdrix, F. Quéré, P. Monot, M. Bougeard, H. Lagadec, P. Martin *et al.*, Double plasma mirror for ultrahigh temporal contrast ultraintense laser pulses, Opt. Lett. **32**, 310 (2007).

[32] C. Rödel, D. an der Brügge, J. Bierbach, M. Yeung, T. Hahn, B. Dromey, S. Herzer, S. Fuchs, A. G. Pour, E. Eckner, M. Behmke, M. Cerchez, O. Jäckel, D. Hemmers, T. Toncian, M. C. Kaluza, A. Belyanin, G. Pretzler, O. Willi, A. Pukhov, M. Zepf, and G. G. Paulus, Harmonic Generation from Relativistic Plasma Surfaces in Ultrasteep Plasma Density Gradients, Phys. Rev. Lett. **109**, 125002 (2012).

[33] F. Quéré, C. Thaury, P. Monot, S. Dobosz, P. Martin, J.-P. Geindre, and P. Audebert, Coherent Wake Emission of High-Order Harmonics from Overdense Plasmas, Phys. Rev. Lett. **96**, 125004 (2006).

[34] A. Leblanc, S. Monchocé, H. Vincenti, S. Kahaly, J.-L. Vay, and F. Quéré, Spatial Properties of High-Order Harmonic Beams from Plasma Mirrors: A Ptychographic Study, Phys. Rev. Lett. **119**, 155001 (2017).

[35] B. Dromey, D. Adams, R. Hörlein, Y. Nomura, S. Rykovanov, D. Carroll, P. Foster, S. Kar, K. Markey, P. McKenna *et al.*, Diffraction-limited performance and focusing of high harmonics from relativistic plasmas, Nat. Phys. **5**, 146 (2009).

[36] H. Vincenti, S. Monchocé, S. Kahaly, G. Bonnaud, P. Martin, and F. Quéré, Optical properties of relativistic plasma mirrors, Nat. Commun. **5**, 3403 (2014).

[37] http://blast.lbl.gov/blast-codes-warp.

[38] https://picsar.net.

[39] J.-L. Vay, R. Lehe, H. Vincenti, B. Godfrey, I. Haber, and P. Lee, Recent advances in high-performance modeling of plasma-based acceleration using the full pic method, Nucl. Instrum. Methods Phys. Res. **829**, 353 (2016).

[40] H. Vincenti and J.-L. Vay, Detailed analysis of the effects of stencil spatial variations with arbitrary high-order finite-difference maxwell solver, Comput. Phys. Commun. **200**, 147 (2016).

[41] G. Blaclard, H. Vincenti, R. Lehe, and J.-L. Vay, Pseudospectral maxwell solvers for an accurate modeling of doppler harmonic generation on plasma mirrors with particle-in-cell codes, Phys. Rev. E **96**, 033305 (2017).

[42] H. Vincenti, M. Lobet, R. Lehe, R. Sasanka, and J.-L. Vay, An efficient and portable simd algorithm for charge/current deposition in particle-in-cell codes, Comput. Phys. Commun. **210**, 145 (2017).

[43] H. Vincenti and J.-L. Vay, Ultrahigh-order maxwell solver with extreme scalability for electromagnetic pic simulations of plasmas, Comput. Phys. Commun. **228**, 22 (2018).

[44] L. Fedeli, A. Sainte-Marie, N. Zaïm, M. Thévenet, J.-L. Vay, A. Myers, F. Quéré, and H. Vincenti, Probing Strong-Field qed with Doppler-Boosted Petawatt-Class Lasers, Phys. Rev. Lett. **127**, 114801 (2021).